Proc. R. Soc. Lond. A **404**, 35–54 (1986)
Printed in Great Britain

Failure characteristics of short anchor bolts embedded in a brittle material

BY R. BALLARINI[1], S. P. SHAH[2] AND L. M. KEER[2]

[1] *Department of Civil Engineering, Cleveland State University, Cleveland, Ohio* 44115, *U.S.A.*

[2] *Department of Civil Engineering, Northwestern University, Evanston, Illinois* 60201, *U.S.A.*

(*Communicated by I. N. Sneddon, F.R.S. – Received* 24 *May* 1985)

[Plate 1]

The results of an analytical and experimental investigation into the failure mechanisms caused by short anchor bolts, embedded in a brittle matrix and loaded monotonically in tension, are presented and discussed. Several engineering applications are included which describe the limitations of currently available design procedures. A mathematical model, based on linear elastic fracture mechanics, is used to predict crack paths, determine the stability of the crack growth, and obtain the tensile capacity of the anchor bolts. The theoretical results are consistent with those obtained from experiments conducted with the use of mortar as a matrix material.

1. INTRODUCTION

The pull-out failure of rigid anchors embedded in brittle (tension-weak) materials is a critical consideration for many design situations. Anchor bolts are often used as connections in concrete structures, roof bolts in rock tunnels and tie backs in rocks. Because failure may occur as a result of the bolts pulling out of the matrix, one of the considerations important for design is the pull-out capacity of the bolts. Klinger & Mendonca (1982) performed a literature review on the tensile capacity of short anchor bolts, where the results of available tensile tests were compared with predictions of six design procedures currently available for computing the nominal capacity of tension-loaded short anchor bolts and welded studs. When an anchor bolt fails by pull-out of the concrete, the resistance is calculated by using either of the following two criteria:

(1) the failure resistance is the resultant of tensile stresses equal to the maximum concrete tensile strength, directed perpendicular to the surface area of the truncated cone shown in figure 1. The angle θ is assumed and varies from 25° (for shallow embedments) to 45° (for deep embedments);

(2) the failure resistance is the resultant of tensile stresses equal to the maximum concrete tensile strength, directed parallel to the direction of the applied load.

Klinger & Mendonca showed that these methods are not conservative and reveal considerable scatter. Their investigation suggests that more accurate procedures are necessary to predict safely the ultimate capacity of anchor bolts.

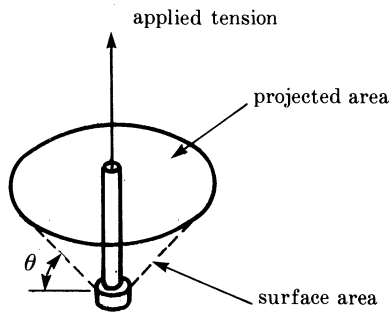

FIGURE 1. Failure surface used in currently available design procedures.

A second application of short anchor bolts is their use in the pull-out test. The strengthening of concrete with time is usually measured by testing field-cured concrete cylinders in uniaxial compression. However, the concrete in a test cylinder may differ significantly from that in the structure because of different transport, casting, compaction, and curing conditions. Considerable interest has recently been directed towards determining *in situ* concrete properties, and among the many non-destructive techniques being investigated, the pull-out test appears to offer promise. The increasing importance of the pull-out test has manifested itself as a tentative standard (ASTM-C900-78T).

One of the more common types of pull-out tests (also called Lok-Test) is shown in figure 2. A test bolt, consisting of a stem and a circular steel disc, is mounted inside the form during construction (figure 2*a*). After curing, the form is stripped and the stem is unscrewed. A rod having a slightly smaller diameter than the stem is screwed into the disc at the time of testing, and a cylindrical counter pressure is applied (figure 2*b*). The rod is then loaded by a pull-out force until failure occurs. Because of its shape, the steel insert pulls out a cone of concrete. The precise geometry of the failure surface depends on factors such as the diameter of the disc, the diameter of the counter pressure, the depth of the embedment and the

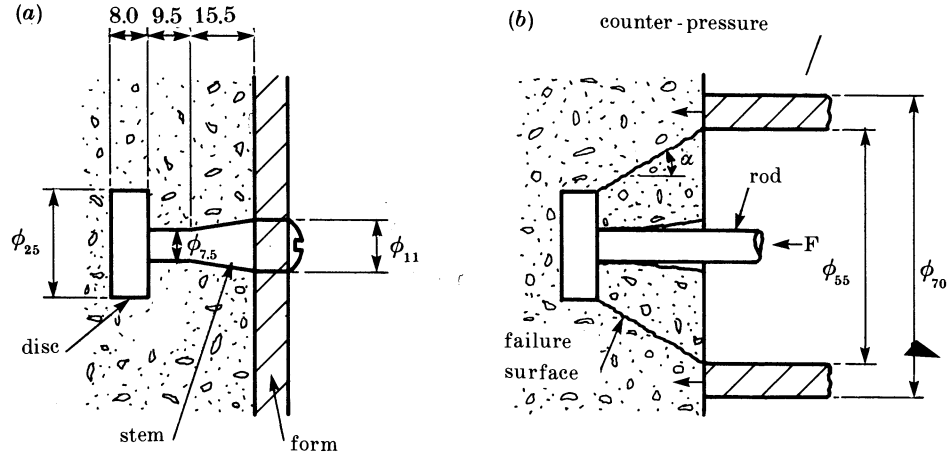

FIGURE 2. Configuration of the Lok-Test. (All dimensions in millimetres.)

constitutive properties of the concrete. The test is considered non-destructive because the damage induced by the relatively small pull-out cone does not impair the integrity of the structural member and can be easily repaired.

The maximum pull-out load is empirically related to the compressive strength. Such calibration curves have been derived from a large number of laboratory and field studies (Malhotra & Carette 1980; Bickley 1981; Kierkgaard-Hansen 1975; Mailhot *et al.* 1979). By correlating standard cylinder strength with the pull-out force at 18 construction sites, Bickley concluded that the empirical relation between pull-out force and compressive strength should be determined for each site and for each type of concrete and aggregate size. One of the reasons for such recommendations, which require extensive empirical calibration, is that the material properties measured by the pull-out test are not sufficiently understood to allow analysis and prediction of the failure mechanisms.

This paper presents a linear elastic fracture mechanics model which can be used to characterize the failure mechanisms of short anchor bolts, and to explain the strength property actually measured by the pull-out test. To simplify the analysis and the experimental procedure, a two-dimensional mathematical model and experimental set-up were selected. The authors believe that the qualitative features of the results and consequently many of the conclusions can be carried over to the axisymmetric situation.

2. Previous investigations

Theoretical investigations into the failure characteristics of the pull-out test have recently been conducted. Ottosen (1981) analysed the Lok-Test by means of axisymmetric nonlinear finite elements. His analysis followed the progression of *circumferential and radial cracking by means of an iterative* smeared cracking procedure, and showed that circumferential cracks begin at the disc edge and grow towards the reaction ring. In addition, Ottosen observed that large compressive stresses run from the disc edge in a rather narrow band towards the support. He postulates that these compressive struts constitute the load-carrying mechanism, and that the failure in pull-out tests is caused by crushing of concrete and not by cracking of concrete. From this he concludes that the test measures compressive strength.

An attempt to show that the Lok-Test is a measure of compressive strength was also made by Jensen & Braestrup (1976), using plasticity theory. They assumed that the failure surface is the frustrum of a cone and that the failure occurs by sliding along this surface. By using the modified Coulomb failure criterion, an upper bound solution was found for the pull-out force. With the geometrical dimensions of the Danish pull-out system, they showed that when the angle between the direction of deformation and the failure surface is equal to the angle of friction for the concrete, then the pull-out force is directly proportional to the concrete compressive strength. Their results, when compared with tests conducted at the Technical University of Denmark, underestimated the experimentally observed pull-out loads.

Realizing the importance of the pull-out test for the safety of concrete structures

during construction, and recognizing that insufficient information exists for the exact failure mode in pull-out tests, Stone & Carino (1983) from the National Bureau of Standards (N.B.S.) conducted pull-out tests on enlarged, extensively instrumented specimens. To circumvent the problems of instrumenting the commercially available pull-out units, which are dimensionally small, the N.B.S. tested specimens which were twelve times as large as those in a standard pull-out test. Strains were measured at various points along the conical surface that joins the edge of the disc and the reaction ring. The internal strains along this surface were measured in three mutually perpendicular directions by specially designed micro-embedment strain gauges. The slip between the bottom of the disc and the surrounding concrete was measured with a slip gauge.

The N.B.S. study is quite important because it represents the first time that detailed measurements were made of internal strains and slip at various stages of the pull-out test. Some of the results are summarized as follows.

(1) Three distinct phases of pull-out behaviour were observed. Circumferential cracking near the upper edge of the disc initiates at about 30–40 % of the ultimate load and ends the elastic response. The circumferential crack continues to grow towards the reaction ring with an increase in load, and any resistance to additional load is provided by aggregate interlock.

(2) Observed compressive strains adjacent to the failure surface were insufficient to initiate compressive failure.

(3) Large tensile strains perpendicular to the failure surface exist near the outer edge of the disc and decrease rapidly towards the reaction ring just before the load at which circumferential cracks initiate. As circumferential cracking progresses, all radial gauges pick up large tensile strains.

The results of the N.B.S. study clearly indicate that stress concentration, crack initiation and crack growth play an important role in determining the pull-out response of concrete. The conclusions from the investigations described above also seem contradictory. Ottosen concludes that the test measures compressive strength, Jensen & Braestrup conclude it measures compressive strength for a certain kinematical condition, while the N.B.S. investigators suggest that a significant amount of finite cracking dominates the failure mechanism.

A more recent experimental investigation to study fracture processes was conducted by Krenchel & Shah (1985). They performed pull-out tests which were in scale with standard equipment. To register micro-cracking in concrete, acoustic emission (a.e.) activity was measured during the test. Some tests were performed with only partial loading, followed by unloading, making it possible to examine the development of microcracking at various load levels by cutting sections of the unloaded concrete specimens. The following conclusions were drawn by the authors.

(1) Crack initiation starts at about 30 % of the maximum load.

(2) For loads up to about 65 % of the peak load, cracking seems primarily concentrated near the upper corners of the pull-out disc. The angle these cracks make with the horizontal (θ) is approximately 15–20°. This cracking system, which appears to be stable, is termed primary cracking.

(3) For loads near the peak load, secondary cracks form ($\theta = 25$–$45°$), running from the upper edge of the disc to the inside edge of the support ring. This secondary cracking pattern did not fully develop all the way around before the peak load was reached.

The Krenchel & Shah study, which is the axisymmetric counterpart of the experiments conducted in the present investigation, can be used for comparison.

In the present investigation a somewhat different approach to determine the failure mechanisms in a pull-out test was applied. Because experiments have shown that failure in the pull-out test is dominated by the propagation of a single crack, fracture mechanics concepts were used to characterize these mechanisms for short anchor bolts. Fracture mechanics concepts have been used to predict crack growth in rock-breaking processes (Ryhming *et al.* 1980).

3. Analysis

The analysis relies on the solution obtained by Ballarini (1985) to the idealized elastostatics problem (figure 3). In the two-dimensional analysis, the anchor is modelled as a vertically loaded, partly bonded rigid plate in an elastic half-space.

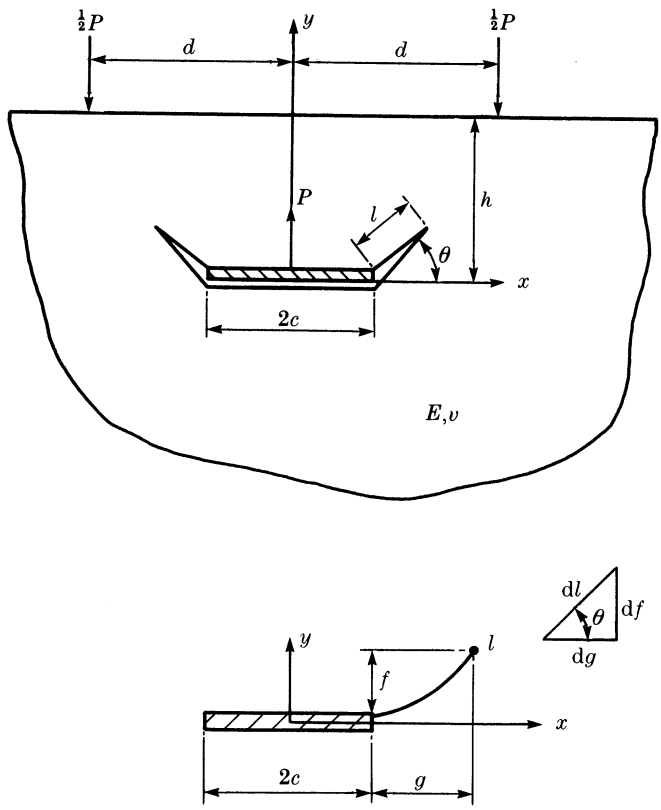

Figure 3. Mathematical model of embedded anchor.

Failure is assumed to arise from cracking which emanates from the corners of the plate. The boundary conditions along the plate corresponding to this problem are

$$2\mu\left(\frac{\partial u}{\partial x}+\mathrm{i}\frac{\partial v}{\partial x}\right)^{+}=0 \quad \text{(bonded upper portion)}, \tag{3.1}$$

and

$$(\sigma_{yy}-\mathrm{i}\sigma_{xy})^{-}=0 \quad \text{(unbonded lower portion)}, \tag{3.2}$$

where u, v are displacements in the x, y directions and σ_{xx}, σ_{xy} and σ_{yy} are components of the stress tensor. Superscripts $+(-)$ refer to the upper (lower) surfaces of the plate, respectively. Along the growing cracks, the required condition is that

$$\sigma_{\phi\phi}-\mathrm{i}\sigma_{\rho\phi}=0 \quad \text{(stress-free crack surface)}, \tag{3.3}$$

where $\sigma_{\phi\phi}$ and $\sigma_{\rho\phi}$ represent the normal and shear stresses along the crack surfaces.

By using Green's functions for a concentrated force in a half-space and for a dislocation in a half-space, together with complex analysis techniques, the elasticity problem is reduced to solving numerically the following system of coupled singular integral equations, whose form is given symbolically here but in detail in Ballarini (1985),

$$\int_0^c \alpha(\xi)\,K_1(x,\xi)\,\mathrm{d}\xi+\int_0^c \beta(\xi)\,K_2(x,\xi)\,\mathrm{d}\xi+\int_0^l \psi(\tau)\,K_3(x,\tau)\,\mathrm{d}\tau$$
$$+\int_0^c \overline{\alpha(\xi)}\,K_{10}(x,\xi)\,\mathrm{d}\xi+\int_0^c \overline{\beta(\xi)}\,K_{11}(x,\xi)\,\mathrm{d}\xi+\int_0^l \overline{\psi(\tau)}\,K_{12}(x,\tau)\,\mathrm{d}\tau+f_1(x)=0;$$
$$0\leqslant x\leqslant c, \tag{3.4}$$

$$\int_0^c \alpha(\xi)\,K_4(x,\xi)\,\mathrm{d}\xi+\int_0^c \beta(\xi)\,K_5(x,\xi)\,\mathrm{d}\xi+\int_0^l \psi(\tau)\,K_6(x,\tau)\,\mathrm{d}\tau$$
$$+\int_0^c \overline{\alpha(\xi)}\,K_{13}(x,\xi)\,\mathrm{d}\xi+\int_0^c \overline{\beta(\xi)}\,K_{14}(x,\xi)\,\mathrm{d}\xi+\int_0^l \overline{\psi(\tau)}\,K_{15}(x,\tau)\,\mathrm{d}\tau+f_2(x)=0;$$
$$0\leqslant x\leqslant c, \tag{3.5}$$

$$\int_0^c \alpha(\xi)\,K_7(t,\xi)\,\mathrm{d}\xi+\int_0^c \beta(\xi)\,K_8(t,\xi)\,\mathrm{d}\xi+\int_0^l \psi(\tau)\,K_9(t,\tau)\,\mathrm{d}\tau$$
$$+\int_0^c \overline{\alpha(\xi)}\,K_{16}(t,\xi)\,\mathrm{d}\xi+\int_0^c \overline{\beta(\xi)}\,K_{17}(t,\xi)\,\mathrm{d}\xi+\int_0^l \overline{\psi(\tau)}\,K_{18}(t,\tau)\,\mathrm{d}\tau+f_3(t)=0;$$
$$0\leqslant t\leqslant l. \tag{3.6}$$

Equations (3.4)–(3.6) are coupled singular integral equations with Cauchy type singularities which satisfy boundary conditions (3.1)–(3.3). The following equations must also be satisfied to ensure a unique solution:

$$\int_0^c [\alpha(\xi)-\overline{\alpha(\xi)}]\,\mathrm{d}\xi=\frac{P}{2\pi\mathrm{i}(\kappa+1)} \quad \text{(equilibrium of plate)}, \tag{3.7}$$

$$\int_0^c [\beta(\xi)-\overline{\beta(\xi)}]\,\mathrm{d}\xi+\int_0^l [\psi(\tau)-\overline{\psi(\tau)}]\,\mathrm{d}\tau=0 \quad \text{(crack closure)}, \tag{3.8}$$

where an overbar denotes complex conjugate and

$$\left.\begin{aligned}\alpha(\xi) &= \frac{-1}{2\pi(\kappa+1)}\frac{\partial}{\partial\xi}(F_x+\mathrm{i}F_y),\\ \beta(\xi) &= \frac{\mu\mathrm{e}^{\mathrm{i}\theta}}{\pi\mathrm{i}(\kappa+1)}\frac{\partial}{\partial\xi}\{[u_r]+\mathrm{i}[v_\theta]\},\\ \psi(\tau) &= \frac{\mu\mathrm{e}^{\mathrm{i}\theta}}{\pi\mathrm{i}(\kappa+1)}\frac{\partial}{\partial\tau}\{[u_r]+\mathrm{i}[v_\theta]\},\end{aligned}\right\} \tag{3.9}$$

with $[u_r]$ and $[v_\theta]$ representing the magnitudes of the displacement jumps and F_x and F_y representing the x and y components of the concentrated force. The details of functions $K_1 \ldots K_{18}, f_1, f_2, f_3$ are given in Ballarini (1985).

All physical quantities can be obtained after solving numerically the equations (3.4)–(3.8). In particular, the stress intensity factor, defined by

$$K_{\mathrm{I}}-\mathrm{i}K_{\mathrm{II}} = \lim_{\tau\to l^+}\sqrt{[2\pi(\tau-l)]}\,(\sigma_{\phi\phi}-\mathrm{i}\sigma_{\phi\phi}) \tag{3.10}$$

can be directly related to the dislocation density $\psi(\tau)$ by taking the asymptotic form of (3.6). In terms of dimensionless quantities arising from the numerical scheme, the result is

$$(K_{\mathrm{I}}-\mathrm{i}K_{\mathrm{II}})\,(c^{\frac{1}{2}}/P) = 2^{\frac{1}{2}}\pi^{\frac{3}{2}}\mathrm{e}^{-\mathrm{i}\theta}\sqrt{(l/c)}\overset{*}{\psi}(1), \tag{3.11}$$

where

$$\psi(\tau) = \frac{\overset{*}{\psi}(s)}{(1-s^2)^{\frac{1}{2}}}\frac{P}{c}; \quad s = \frac{2\tau}{l}-1. \tag{3.12}$$

4. Pre-cracking solution

Computations were first performed to calculate the stress fields before crack initiation. Plane strain was assumed and Poisson's ratio was assumed to be equal to 0.2 for all numerical results.

The minimum principal stresses (maximum compressive), defined by

$$\sigma_2 = \tfrac{1}{2}(\sigma_{xx}+\sigma_{yy})-\sqrt{[(\tfrac{1}{2}\sigma_{xx}-\sigma_{yy})^2+\sigma_{xy}^2]}, \tag{4.1}$$

are plotted in figures 4 and 5. It can be seen from these figures that the location of the concentrated forces influences significantly the stress fields. For both cases very high stresses are seen near the edges of the pull-out disc. Without concentrated forces (figure 5) the compressive stresses decay rapidly with distance from the edges of the disc. With concentrated forces present (figure 4), high compressive stresses exist in a region extending from the tips of the anchor to the location of the concentrated forces. These results confirm the existence of the compressive struts observed in the finite element work of Ottosen, but the magnitudes of these stresses are not sufficiently large to cause crushing of the concrete. The values of $\sigma_2 c/P$ in the compressive struts are approximately 1.0. Assuming values of c and P equal

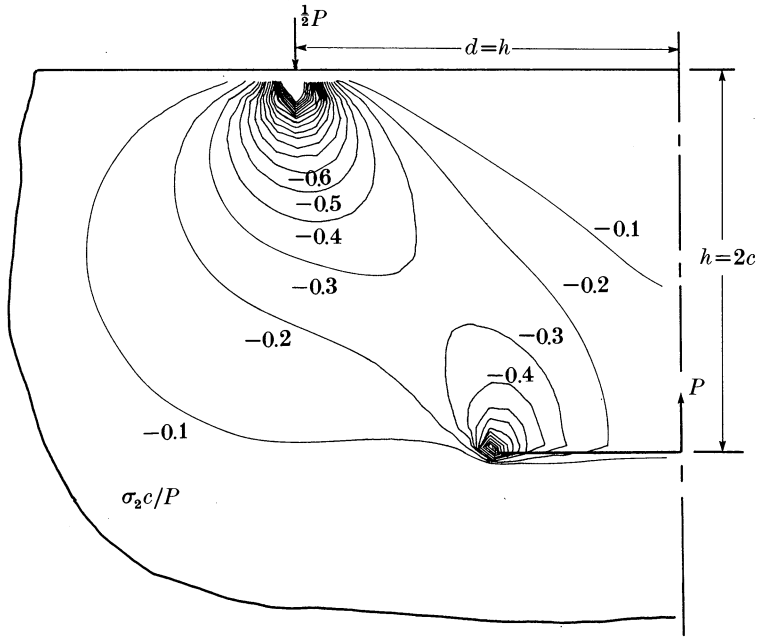

FIGURE 4. Contours of minimum principle stresses (concentrated forces present).

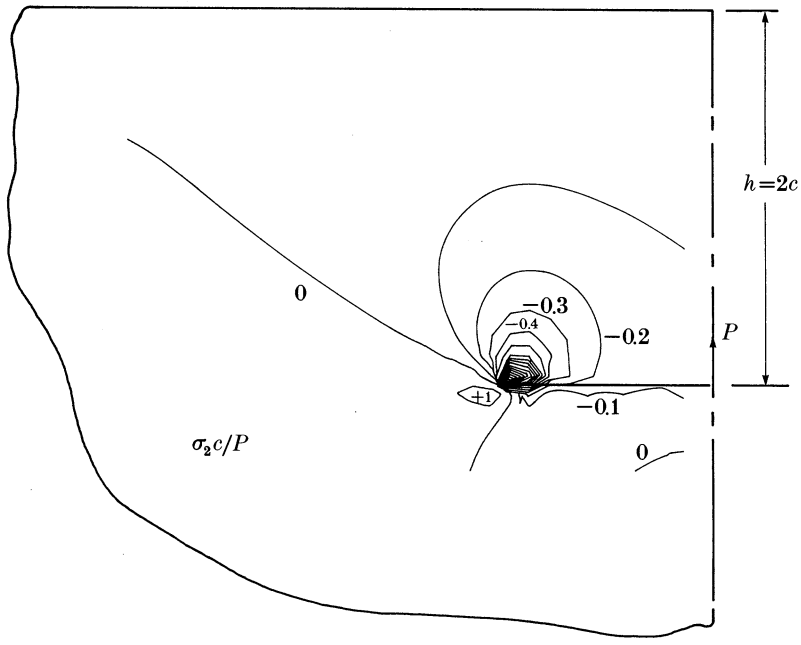

FIGURE 5. Contours of minimum principle stresses (concentrated forces *not* present).

to $\frac{1}{2}$ in†, and 1000 lbs‡ in^{-1}, respectively (these values correspond to those observed in the experiments to be reported later), a maximum compressive stress equal to 2000 p.s.i. would result, which is less than the compressive strength of most concretes. The conclusion made by the N.B.S. investigators that the observed compressive strains adjacent to the failure surface were insufficient to initiate compressive failure is therefore confirmed.

5. Stress intensity factor analysis

To characterize crack growth during the pull-out process, stress intensity factors were calculated for several combinations of the parameters involving crack length, angle of extension, location of the concentrated forces support reactions at the top surface, and embedment depth of the plate. Figures 6–11 present the results of these calculations.

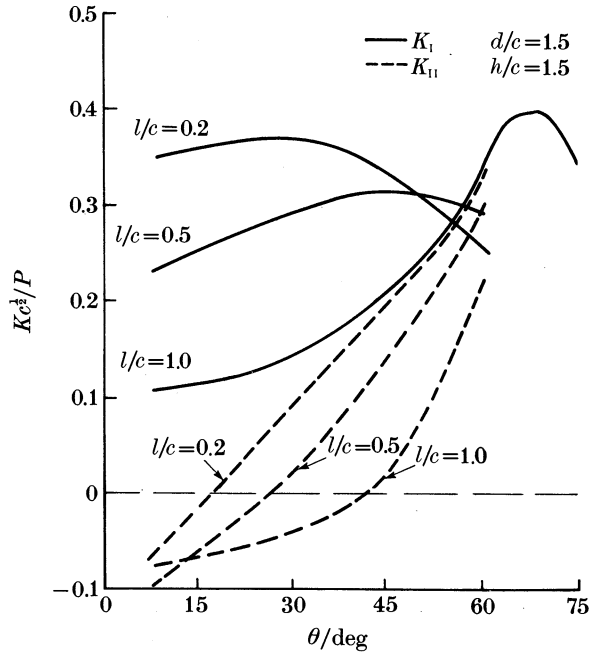

Figure 6. Stress intensity factors as functions of extension angle (concentrated forces present).

Figures 6 and 7 are plots of the stress intensity factors as functions of the crack extension angle for two configurations. The results show that for short cracks the maximum values of the opening-mode stress intensity factor (K_I) occur at points where the shear-mode factor (K_{II}) is nearly zero. We assume that both crack initiation and the direction that the extended crack will choose to grow are governed by the opening mode (see, for example, Horii & Nemat-Nasser 1985).

† 1 in = 2.54×10^{-2} m. ‡ 1 lb = 0.45359237 kg.

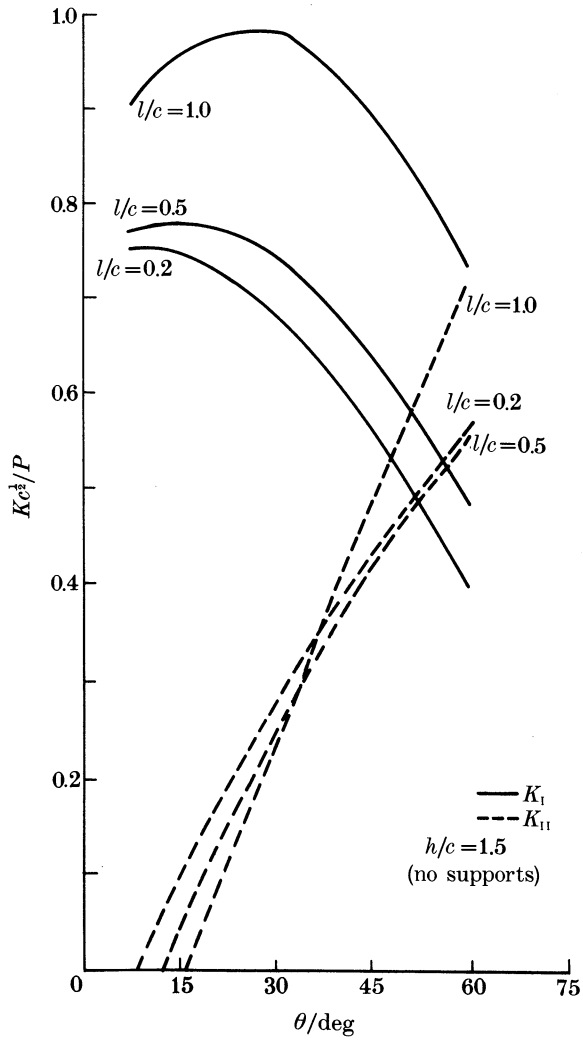

FIGURE 7. Stress intensity factors as functions of extension angle (concentrated forces not present).

The anchor pull-out crack initiation direction will therefore be assumed to depend upon the direction of *maximum* K_{I}.

Figure 8 is a plot showing the maximum value of the opening-mode stress intensity factor versus crack length for several test configurations. The effect that the support reactions have on the stability of crack propagation can be clearly seen. For relatively short spacing of the support forces and deep embedments, cracks will grow in a stable manner (an increase in load is needed for additional growth) until they reach l/c values approximately equal to 0.75; after this point they will continue to grow, but in an unstable manner. On the other hand, for wide spacing and shallow embedments, crack growth is unstable for all crack lengths. The

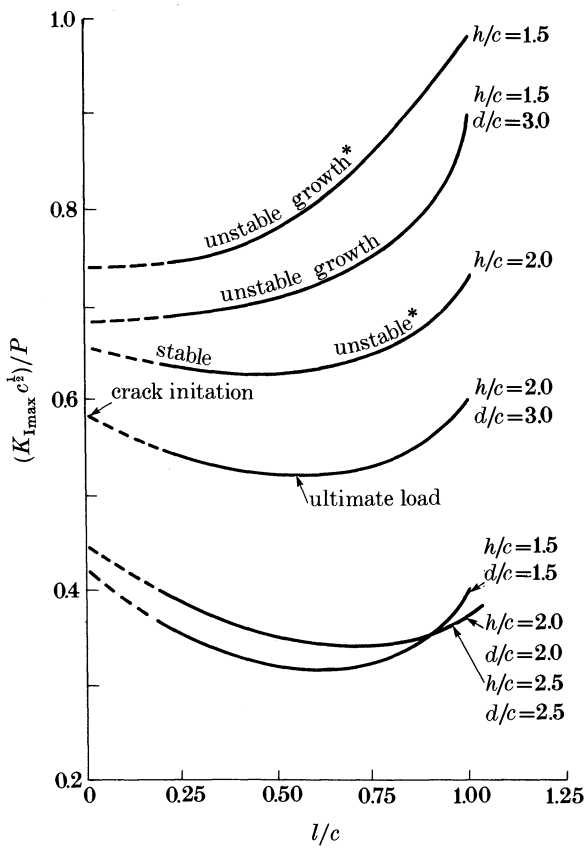

FIGURE 8. Maximum mode I stress intensity factors as functions of crack length (asterisk indicates no supports).

configurations of the Lok-Test and of Krenchel & Shah's test set-up correspond to the case where $d/c = h/c = 2.0$. These results therefore explain the stable crack propagation that was observed in their experiments.

The approximate method proposed by Horii & Nemat-Nasser was used in this study to predict crack paths. With respect to the xy coordinate system shown in figure 3, let the crack profile be defined by $x = c+g(r)$, $y = f(r)$, where r is a parameter that measures length along the crack, and c is the half-length of the plate. Figure 9 is a plot obtained from results such as those in figures 6 and 7 showing the angles for maximum K_{I} as functions of crack length for several configurations. The angle between the tangent to the curved crack extension and the x axis is assumed to be $\theta = \theta(l/c)$, so that

$$\mathrm{d}f/\mathrm{d}l = \sin\theta, \quad \mathrm{d}g/\mathrm{d}l = \cos\theta. \tag{5.1}$$

The crack profiles shown in figures 10 and 11, were obtained after numerically integrating (5.1), into which $\theta(l/c)$ from figure 9 was substituted.

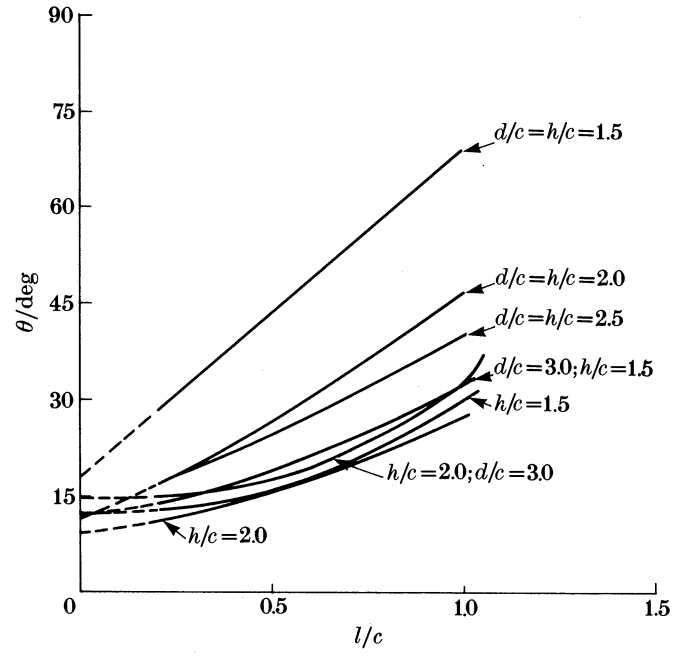

FIGURE 9. Angles for which K_I is maximum as functions of crack length.

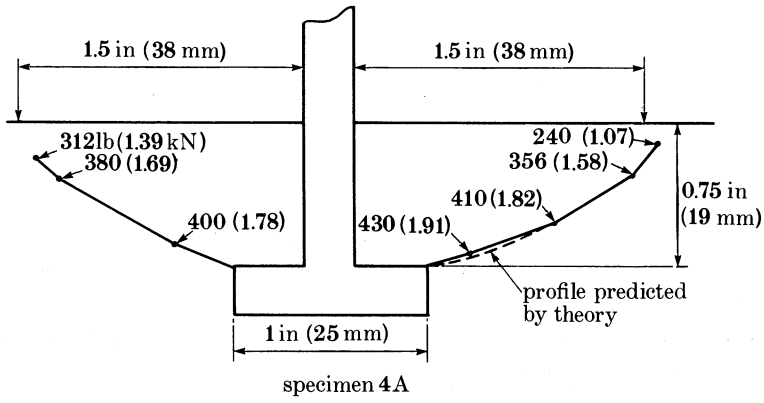

FIGURE 10. Experimentally observed and theoretically predicted crack profiles (load levels in experiments designated at various points, in pounds (kilonewtons)).

It can be seen that cracks will initiate and grow almost horizontally for short lengths; for $l/2c = 0.1$, θ varies from 10 to 25°, depending on the embedment depth and the spacing of the concentrated forces. As the cracks become longer, they tend to turn and grow towards the supports. These statements will be tested by the experimental programme described in §6.

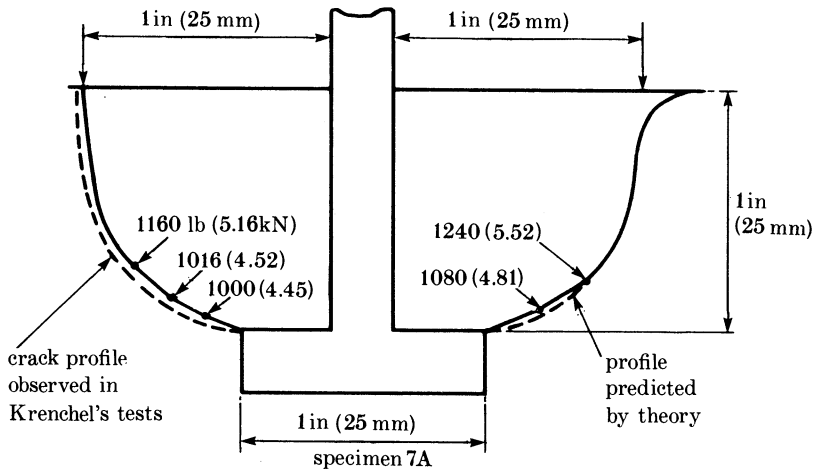

FIGURE 11. Experimentally observed and theoretically predicted crack profiles.

6. EXPERIMENTAL PROGRAMME

In this section the procedure and results of an experimental investigation conducted to validate the predictions of the analytical model are described. Tests were conducted by using mortar as a matrix material. In practice, the configurations of the pull-out test and anchor bolts are axisymmetric, but because the crack path cannot be observed for an axisymmetric test in an opaque material, the planar system shown in figure 12 was used. By using this system, crack propagation can be monitored throughout the experiment (on the surface of the specimens). To determine the influence of geometry the embedment depth and the spacing of the support reactions were varied, and to determine the influence of compressive strength the tests were performed for three ages of curing: 1, 2, and 3 days.

The objective of this investigation was to determine the effect of geometry on the failure characteristics of embedded anchors; therefore, only one mix was used in the experimental investigation. The mix proportions of the mortar were 1:2:0.5 (cement:sand:water) by mass. Type I Portland cement was used.

The 6 in × 6 in × 1.75 in specimens and 3 in × 6 in cylinders were cast in individual moulds, were kept in their formwork for 24 h, and were covered by plastic to avoid moisture loss. After 24 h the specimens and cylinders which did not have to be tested after the first day were removed from their moulds and placed in a humidity room to aid curing and to deter shrinkage crack formation. The specimens and cylinders were kept in the moisture room until an hour before testing.

Compression tests were performed on two cylinders one hour before testing to determine the compressive strength of the mix. The compressive strengths, which were recorded and used in subsequent calculations, represent the average of the two tests.

The reaction frame and the support rollers and frictionless blocks are shown in figure 13, plate 1. The frictionless blocks were used to prevent rotation of the anchor and to ensure that the anchor would pull out vertically. As an added safety

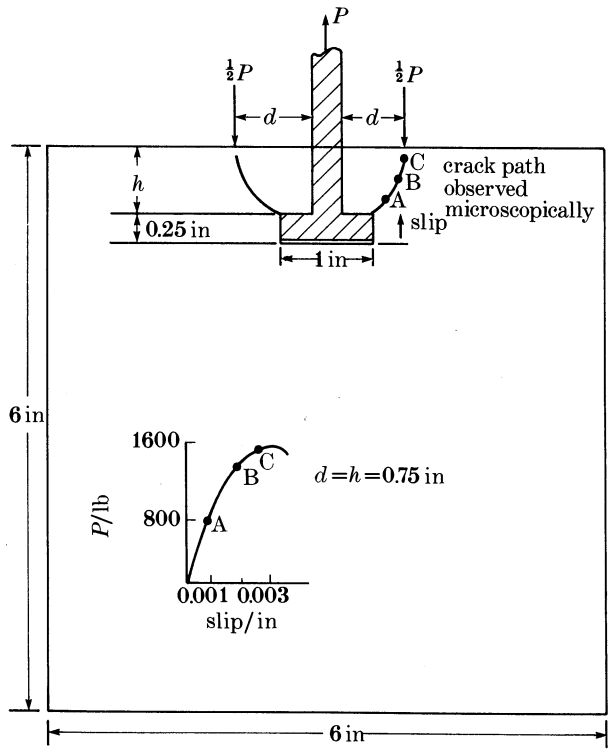

FIGURE 12. Configuration of planar pull-out test specimen (variables: d, h, matrix properties).

precaution $\frac{1}{8}$ in thick compressible mounting tape covered with oil was placed on the sides and bottom of the anchor and on the anchor stem to produce a debond between the bottom of the anchor and the surrounding concrete. These precautions enabled consistently symmetric crack growth to occur and a reasonably close match to the analytical configuration was assumed. In a preliminary pilot programme these precautions were not taken, and antisymmetric unstable crack growth often resulted. A series of tests were also conducted in which the supports were not present. The configuration of these tests is shown in figure 13.

A hydraulic, servo-controlled M.T.S. structural test system with a load capacity of 20 kip† was used for loading. The tests were performed at a stroke rate of 10^{-5} in s^{-1}. The slip of the anchor was recorded with the use of a linear displacement voltage transducer (l.d.v.t.) and crack tip locations were monitored microscopically by using a microscope with 30-fold magnification (figure 13).

A total of 28 tests were performed. The variables in these tests were the embedment depth h, the support reaction distance d, and the age of the specimens (compressive strength). The results are presented in table 1 and figures 14–17. These results clearly show the influence of geometry on the failure mechanisms.

Two typical load–slip curves are presented in figures 14 and 15. The *slip* is the

† 1 kip = 4.448222 kN.

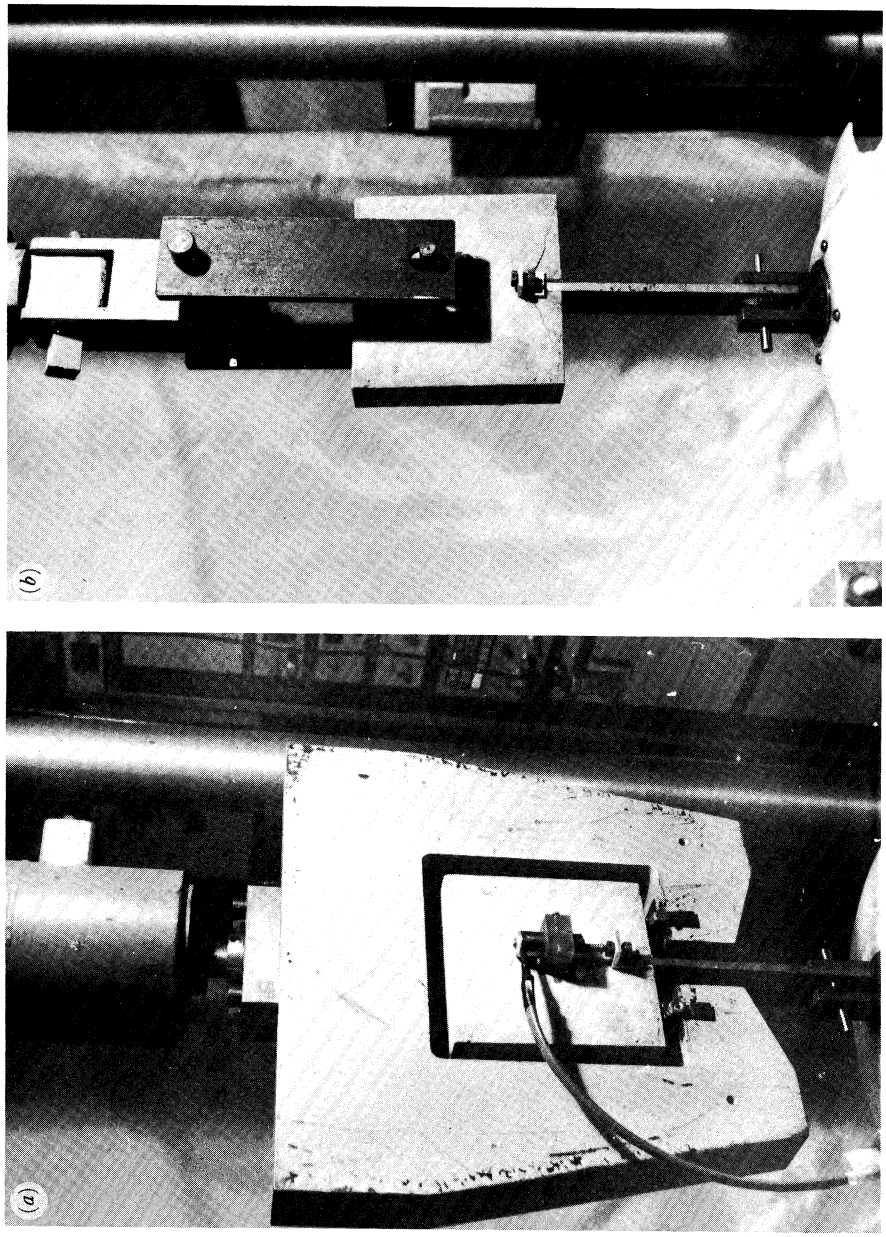

FIGURE 13. Overall view of testing system: (*a*) supports present; (*b*) supports not present.

(*Facing p.* 48)

TABLE 1. INFLUENCE OF GEOMETRY ON FAILURE

series	specimen	configuration d/in	h/in	f'_c/p.s.i.	P_{ult}/lb	P_{crack}/lb
1	1A	0.75	0.75	3063	1180	600
1	1B	0.75	0.75	3063	1220	not observed
1	2A	0.75	0.75	4075	1600	800
1	2B	0.75	0.75	4075	1520	not observed
1	3A	0.75	0.75	4785	1880	not observed
1	3B	0.75	0.75	4785	1680	1000
2	4A	1.5	0.75	3102	450	450
2	4B	1.5	0.75	3102	450	450
2	5A	1.5	0.75	5286	620	620
2	5B	1.5	0.75	5286	580	not observed
2	6A	1.5	0.75	6090	670	670
3	7A	1.0	1.0	4347	1540	1000
3	7B	1.0	1.0	4347	1410	not observed
3	8A	1.0	1.0	4810	1620	1000
3	8B	1.0	1.0	4810	1490	1000
4	9A	1.5	1.0	4053	780	700
4	9B	1.5	1.0	4053	750	not observed
4	10A	1.5	1.0	4792	780	not observed
4	10B	1.5	1.0	4792	840	750
4	11A	1.5	1.0	5800	820	not observed
4	11B	1.5	1.0	5800	860	not observed
5	12A	1.25	1.25	3632	1200	880
5	12B	1.25	1.25	3632	1320	not observed
5	13A	1.25	1.25	4669	1320	not observed
5	13B	1.25	1.25	4669	1400	not observed
6	14		0.75	5118	615	615
6	15		0.75	6027	640	640
6	16		0.75	6543	680	680

relative displacement between the anchor and a point on the concrete 1 in below the anchor. The purpose of these records was to determine the magnitude of the slip and to determine at what percentage of the ultimate load nonlinear response was initiated. A rough check on the microscopic observations of crack initiation was therefore provided by comparing the load levels at which nonlinear displacements were initiated with the load levels at which cracks were microscopically first observed. For the configuration shown in figure 14 cracking was observed at 50 % of the ultimate load. Observation of the load–slip record indicates that a nonlinear response was initiated at this load level. For the configuration shown in figure 15 cracking was observed at the peak load. The nonlinear response was also initiated at peak load.

The slip of the anchor was always very small before cracking initiated (*ca.* 0.001 in); this observation was also made in the experiments conducted by the N.B.S. and by Krenchel & Shah.

Table 1 shows that the ultimate load decreases as the embedment depth decreases or the support distance increases. The results also indicate the loads at which cracking initiated and agree with the predictions of the analytical model. For the configurations corresponding to series 1, 3, 4, and 5, table 1 shows that crack growth is stable as predicted in figure 8. For the configurations corresponding

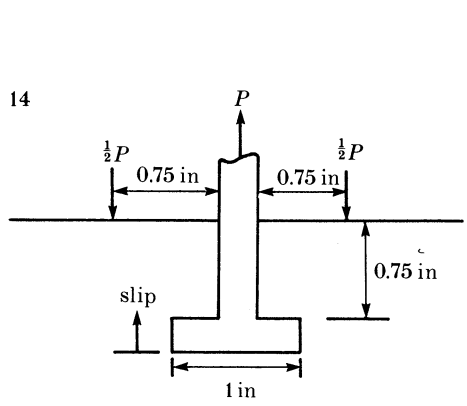

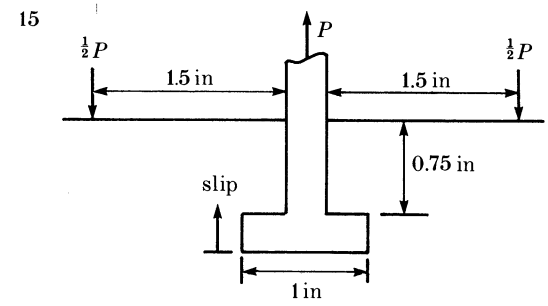

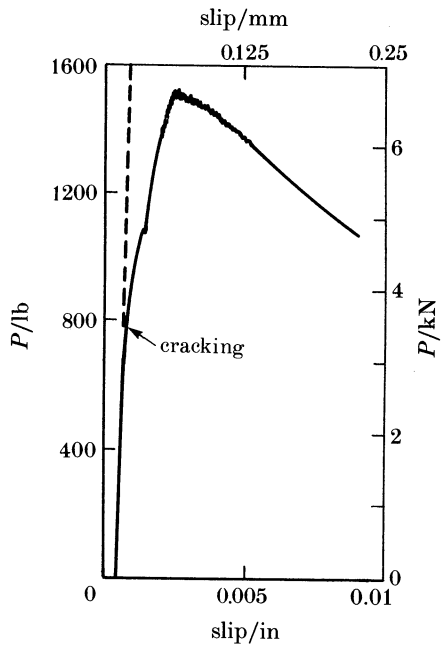

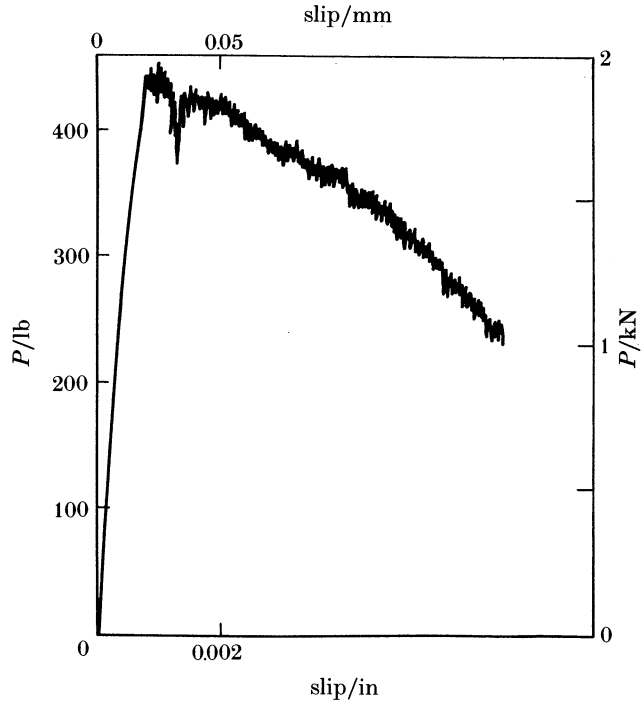

FIGURE 14. Load–slip record (narrow spacing of supports).

FIGURE 15. Load–slip record (wide spacing of supports).

to series 2 and 6, table 1 as well as figure 8 shows that cracks will initiate at peak load.

Figures 10 and 11 are sketches of the crack tip locations as observed through the microscope for two specimens at various load levels. On these the crack paths as predicted by the analytical model are superimposed. The model predicts crack profiles reasonably well.

Figures 16 and 17 show the relation between compressive strength and pull-out load for crack initiation and for ultimate loads. Each curve in these figures represents a geometry-dependent calibration curve for a particular configuration.

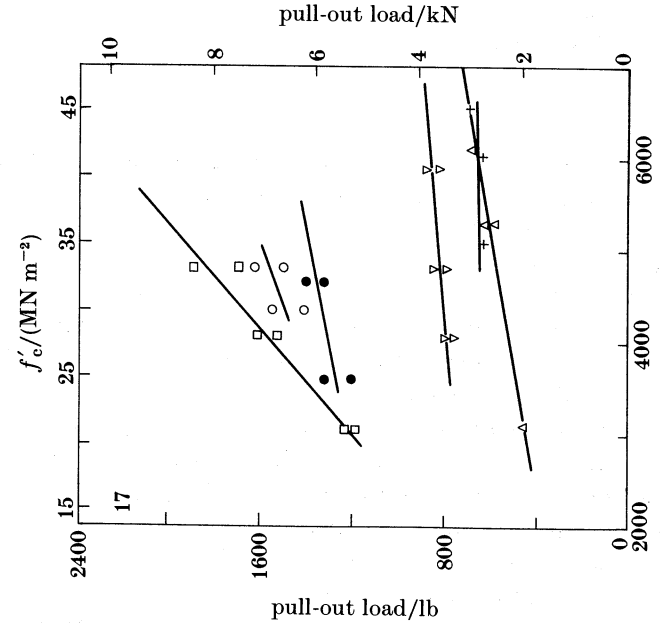

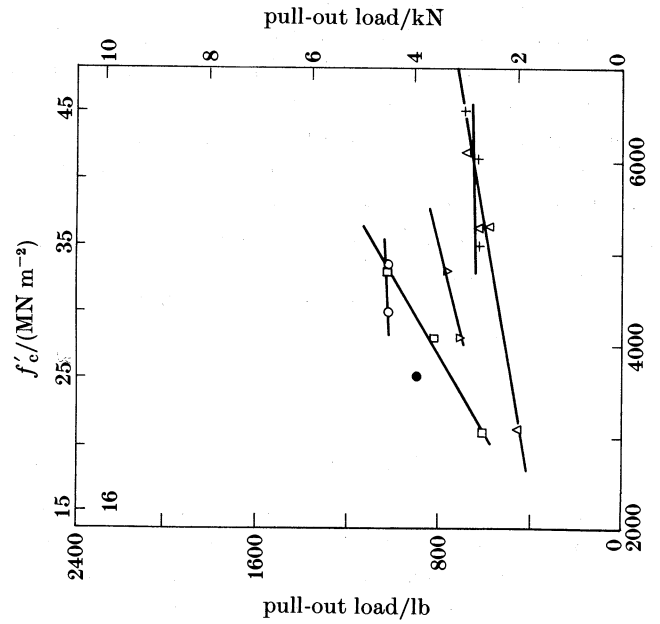

FIGURE 16. Pull-out loads at crack initiation as functions of compressive strength. Series: □ (1), $d = h = 0.75$ in; △ (2), $d = 1.5$ in, $h = 0.75$ in; ○ (3), $d = h = 1$ in; ▽ (4), $d = 1.5$ in, $h = 1$ in; ● (5), $d = h = 1.25$ in; + (6), $h = 0.75$ in.

FIGURE 17. Pull-out loads at ultimate as functions of compressive strength. Dimensions as figure 16.

Fracture mechanics has therefore been shown to characterize qualitatively the failure mechanisms of short anchor bolts. In §7 the model will be used to predict the tensile capacity of anchor bolts.

7. Tensile capacity

The initiation and the ultimate loads obtained in the experiments will now be predicted by the analytical model. The geometrical dependence, which is shown in figures 16 and 17, can be eliminated if the compressive strength is plotted as a function of the fracture toughness, K_{IC}.

Figures 18 and 19 show the critical stress intensity factors as functions of compressive strength for crack initiation (figure 18) and for ultimate loads (figure 19). These figures were constructed by extracting the factor $Kc^{\frac{1}{2}}/P$ from figure 8 at the point of instability for ultimate load and the factor $Kc^{\frac{1}{2}}/P$ at $l/c = 0$ for crack initiation. By multiplying these factors by the experimentally observed ultimate loads and crack-initiation loads (obtained from table 1 and divided by the thickness of the specimen to be consistent with the P in figure 3), the factors $(Kc^{\frac{1}{2}})$ at ultimate load and $(Kc^{\frac{1}{2}})$ at initiation load are obtained and plotted as functions of compressive strength (also obtained from table 1).

It can be seen from these figures that for a particular compressive strength, the fracture toughness lies in a relatively narrow band. The figures imply that the tensile capacity is governed by the fracture toughness. Because these figures are independent of geometry they can be used to predict either ultimate (or crack-initiation) loads given the compressive strength, or compressive strength given the ultimate loads. The former method may be used to determine the tensile capacity of short anchor bolts, while the latter may be used in pull-out testing applications.

It can be seen from figures 18 and 19 that the fracture toughness for a given compressive strength is higher for ultimate loads than for crack-initiation loads and is a result of the so-called process zone which develops in the vicinity of the crack tip when stable crack growth occurs. In this zone, nonlinear deformations (microcracking, aggregate interlock, etc.) occur, increasing the resistance to crack growth and resulting in a higher apparent fracture toughness. If the effect of the process zone were to be incorporated into the model, then there would be negligible discrepancy between figures 18 and 19. Models such as those proposed by Wecharatana & Shah (1983); Jenq & Shah (1985*a*, *b*), and Ballarini *et al.* (1984) can be used to treat the process zone.

8. Conclusions

From the results of this investigation the following conclusions can be drawn.

(1) The tensile capacity of anchor bolts is governed by the fracture toughness of the matrix. By plotting the fracture toughness as a function of compressive strength, the resulting curves are shown to be independent of geometry. These curves can be used either to calculate ultimate loads, knowing the compressive strength (design of anchor bolts), or conversely, to calculate compressive strength knowing the ultimate load (pull-out testing applications).

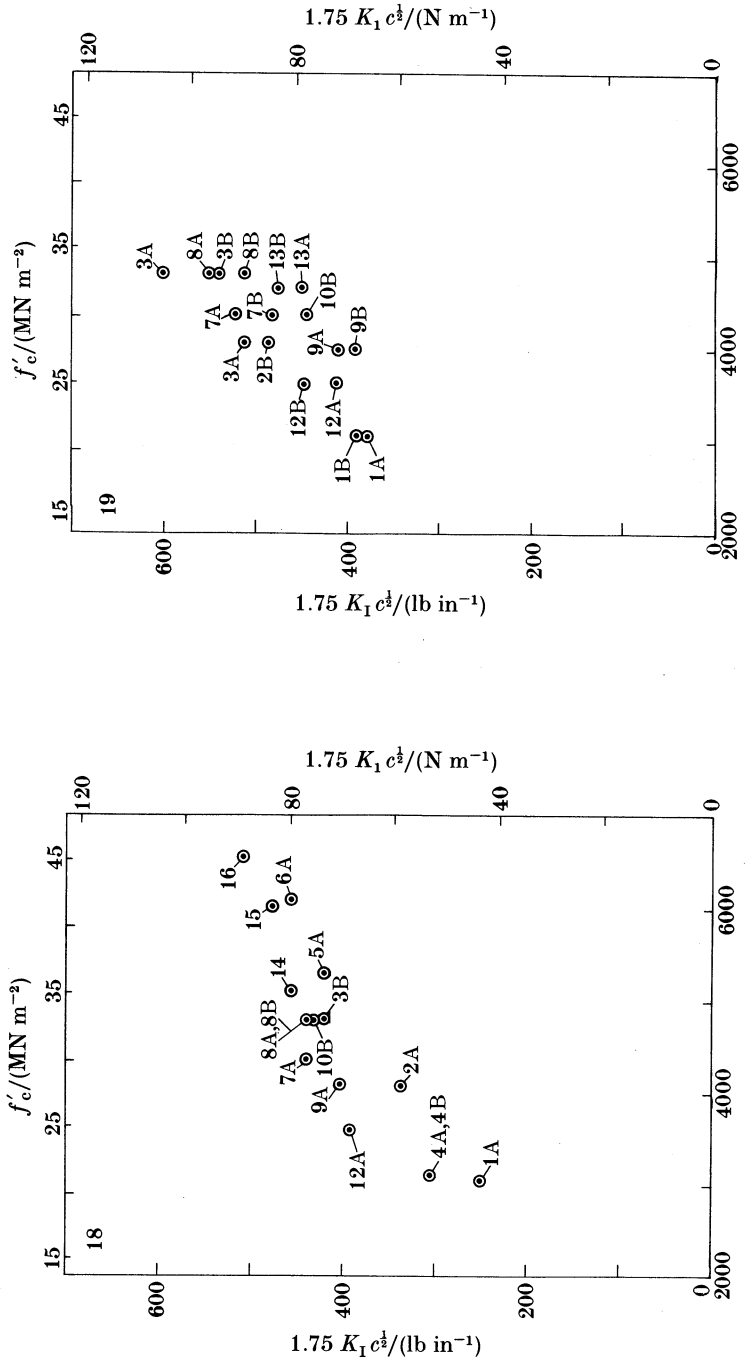

FIGURE 18. Fracture toughness at crack initiation as a function of compressive strength.

FIGURE 19. Fracture toughness at ultimate as a function of compressive strength (only where $P_{ult} > P_{init}$).

(2) Previous methods used to calculate the tensile capacity of short anchor bolts show scatter and are unconservative because they assume a certain tensile resistance equal to the maximum tensile strength of the matrix acting along an assumed failure surface. As shown in this study for the anchor bolt problem, when the supports are not present, crack propagation becomes unstable. The failure surface is a by-product of the fracture process, and does not contribute to the tensile capacity as the currently used design procedures assume. The crack initiation and the ultimate load are governed by the fracture toughness.

(3) For relatively short reaction distances and deep embedments crack propagation is stable, and additional resistance to crack growth is provided by nonlinear deformations occurring in the vicinity of the crack tip. To understand this stage of the failure process, a model which includes the nonlinear deformations such as microcracking, and possibly crack branching, in the vicinity of the main crack tip must be included.

This research investigation was supported by the Air Force Office of Scientific Research under Grant no. AFOSR-82-0243 (Lt Col. Lawrence D. Hokanson, Program Manager).

References

Ballarini, R. 1985 *An analytical and experimental investigation of a two-dimensional anchor pull-out test.* Ph.D. dissertation, Northwestern University.

Ballarini, R., Shah, S. P. & Keer, L. M. 1984 *Engng Fract. Mech.* **20**, 433–445.

Bickley, J. A. 1981 In *In-situ nondestructive testing of concrete* (ed. V. M. Malhotra), pp. 195–198. American Concrete Institute, special vol. SP-82.

Horii, H. & Nemat-Nasser, S. 1985 *J. geophys. Res.* **90**, 3105–3125.

Jenq, Y. S. & Shah, S. P. 1985*a* In *Application of fracture mechanics to cementitious composites* (ed. S. P. Shah), pp. 319–359. Martinus Nijhoff.

Jenq, Y. S. & Shah, S. P. 1985*b* *Engng Fract. Mech.* **21**, 1055–1069.

Jensen, B. C. & Braestrup, H. W. 1976 *Nord. Betong* **20**, 9–11.

Kierkgaard-Hansen, P. 1975 *Nord. Betong* **19**, 19–28.

Klinger, R. E. & Mendonca, J. A. 1982 *J. Am. concr. Inst.*, **79**, 270–279.

Krenchel, H. & Shah, S. P. 1985 *Mater. Struct.* **108** (To be published.)

Mailhot, G., Bisaillon, A., Carette, G. G. & Malhotra, V. M. 1979 *Proc. Am. concr. Inst.* **76**, 1267–1282.

Malhotra, V. M. & Carette, G. G. 1980 *J. Am. concr. Inst.* **77**, 161–170.

Ottosen, N. S. 1981 *J. struct. Div., Am. Soc. civ. Engrs* **107**, 591–603.

Ryhming, I., Cooper, G. A. & Berlie, J. 1980 *Proc. R. Soc. Lond.* A **373**, 331–351.

Stone, W. C. & Carino, N. J. 1983 *J. Am. concr. Inst.* **80**, 501–513.

Wecharatana, M. & Shah, S. P. 1983 *J. Engng Mech. Div., Am. Soc. civ. Engrs* **109**, 1231–1240.